AAS 26-012

# LOS-AWARE BEACON PLACEMENT FOR ROBUST RELATIVE NAVIGATION FOR SPACECRAFT PROXIMITY OPERATIONS

**Ruthvik Bommena*** **and Robyn Woollands†**

Robust relative navigation during spacecraft proximity operations is fundamentally limited by navigation beacon placement, sensor visibility, and complex spacecraft geometries that cause line-of-sight (LOS) occlusions. This paper presents a LOS-aware beacon-placement optimization framework for a conceptual large-aperture space telescope with a cross-shaped sunshield whose perimeter contains a discrete network of mountable rails. To enable gradient-based optimization on this inherently discrete geometry, we introduce a Continuous Surface Parameterization for Discrete Geometry (CSP–DG) formulation that represents each beacon location as a smooth softmax mixture over rail curves, with entropy and diffuseness regularization to promote single-rail convergence. LOS constraints induced by the sunshield and primary mirror are modeled using a union of convex ellipsoids, and visibility is evaluated efficiently and robustly via a constrained-minimum test of the ray–ellipsoid quadratic. Candidate beacon layouts are evaluated by propagating a continuous–discrete Extended Kalman Filter with range measurements and realistic commercial off-the-shelf sensor noise over a tube of 100 approach trajectories, using a worst-case $P_{99}$ position error metric to enforce robustness. Numerical results show that the proposed method converges to a fully discrete seven-beacon layout on the rails that achieves $P_{99} \leq 0.10$ m across all trajectories, outperforming random feasible placements by orders of magnitude.

## INTRODUCTION

The continued growth in interest for in-space servicing, assembly, and manufacturing (ISAM) is driving the development of increasingly complex spacecraft architectures and proximity operations in challenging orbital environments,[1,2] particularly in highly obstructed or deep-space environments, where traditional Global Navigation Satellite System (GNSS) infrastructure is unreliable or unavailable.[3,4] Future missions involving large-aperture space telescopes, modular observatories, and on-orbit infrastructure will rely on autonomous servicing spacecraft to perform inspection, rendezvous, proximity operations, and assembly tasks with high precision and reliability.[5–8] A fundamental enabler of these operations is robust relative navigation, which must provide accurate state estimates despite sparse sensing, limited onboard resources, and complex spacecraft geometries. In many envisioned ISAM missions, relative navigation is achieved using range or bearing-limited measurements from navigation beacons mounted on the target spacecraft, due to their simplicity, scalability, and compatibility with small servicing vehicles.[9,10] However, the effectiveness of such beacon-based navigation systems is critically dependent on beacon placement, sensor visibility, and geometric observability, particularly in the presence of large structural elements that result in frequent line-of-sight (LOS) occlusions. As spacecraft structures grow in size and geometric complexity, systematically designing beacon layouts that remain observable across realistic proximity trajectories becomes a nontrivial and mission-critical challenge.

A growing body of literature has investigated sensor and beacon placement strategies for relative navigation, state estimation, and cooperative localization in space and robotics applications.[11–15] Much of this

*Graduate Student, Department of Aerospace Engineering, University of Illinois Urbana-Champaign, 104 S Wright St, Urbana, IL, USA, 61801.

†Assistant Professor, Department of Aerospace Engineering, University of Illinois Urbana-Champaign, 104 S Wright St, Urbana, IL, USA, 61801.

work, however, relies on simplified geometric assumptions that limit its applicability to large, structurally complex spacecraft. In particular, many existing approaches assume convex or weakly nonconvex target geometries—such as spheres, cylinders, or box-like approximations—or permit beacon placement on continuous surfaces without accounting for discrete, mechanically admissible mounting locations.[15–18] While these assumptions simplify the placement problem and enable elegant analytical results, they do not reflect the realities of modern space telescopes and modular observatories, whose external surfaces are dominated by segmented sunshields, truss elements, mirrors, and appendages.[7] In such systems, navigation hardware can typically be mounted only along a sparse set of structural rails or edges, introducing a fundamentally discrete design space that is poorly handled by conventional continuous formulations. In addition to geometric simplifications, LOS visibility constraints are often neglected or treated in an overly idealized manner.[19] Many beacon-placement studies implicitly assume persistent visibility between the observer and all beacons, or enforce conservative binary visibility rules that are decoupled from the actual spacecraft geometry.[12,19–22] For large-aperture observatories, however, sunshields, primary mirrors, and support structures frequently occlude optical and ranging paths in a highly pose- and trajectory-dependent manner. Ignoring these effects can lead to beacon layouts that appear favorable under simplified models but suffer severe observability loss when deployed on realistic spacecraft.[23] Consequently, there remains a gap in existing literature for beacon-placement methodologies that explicitly incorporate realistic spacecraft geometry, discrete mounting constraints, and LOS occlusions induced by large structural elements.

Beyond geometric modeling, important limitations also arise in how beacon layouts are evaluated and compared. A large fraction of existing work assesses placement quality using local or linearized observability metrics, such as Fisher information matrices,[24,25] observability Gramians,[26] geometric dilution of precision (GDOP),[27] or condition numbers derived from instantaneous measurement Jacobians. While these metrics provide useful insight into local sensing geometry, they do not capture the nonlinear, time-varying behavior of practical state estimators operating under realistic noise, intermittent measurements, and imperfect initialization. In particular, linearized observability measures are typically evaluated at a single operating point or along a nominal trajectory and implicitly assume persistent measurement availability.[10,28] As a result, they can significantly overestimate navigation performance in scenarios where LOS visibility varies along the trajectory or where the observable subspace temporarily collapses due to unfavorable beacon geometry or occlusions. Moreover, relatively few studies evaluate beacon-placement strategies using a full nonlinear filtering framework, such as an Extended Kalman Filter (EKF), propagated over realistic spacecraft trajectories with time-varying visibility and measurement dropouts.[29] When estimation performance is reported, it is often summarized using mean or root-mean-square (RMS) error metrics computed over a single nominal trajectory.[28] Such metrics tend to obscure short-duration but mission-critical error growth events that arise during periods of poor observability, which are especially common in LOS-limited proximity operations around large structures. Even fewer approaches address robustness explicitly by evaluating performance across families of trajectories or by considering tail-error behavior, despite the fact that worst-case estimation errors, rather than average performance, often drive mission risk and operational constraints.[10,29] Consequently, existing beacon-placement methodologies rarely provide guidance on the minimum number of beacons required to satisfy stringent accuracy requirements across a broad set of operational scenarios, leaving a critical gap in optimal and robust beacon placement strategies.

To address these challenges, this paper develops a LOS-aware beacon-placement framework that directly couples geometric design and constraints, visibility constraints, and nonlinear state-estimation performance. Beacon locations are constrained to a discrete set of structural rails on a hypothetical large-aperture space telescope acting as the target spacecraft, reflecting realistic mechanical mounting limitations. These discrete locations are embedded into a smooth optimization space through a Continuous Surface Parameterization for Discrete Geometry (CSP–DG) formulation, which permits efficient gradient-based search. LOS occlusions caused by large structural elements are captured using a compact ellipsoidal approximation of the spacecraft geometry and are explicitly enforced within a continuous–discrete EKF (CD–EKF). At each time step, range measurements from occluded beacons are excluded from the filter update, ensuring that candidate layouts are evaluated based on their true impact on nonlinear estimation performance under time-varying visibility. Robustness is assessed by propagating the CD–EKF across a dense tube of servicing trajectories constructed about multiple fuel-optimal rendezvous solutions generated using a target-relative circular restricted three-

body problem (TR-CRTBP) model.[5] This trajectory ensemble captures realistic variability in approach geometry and induces strongly trajectory-dependent sensing conditions. Beacon layouts are then designed to minimize a worst-case upper-tail estimation error metric, allowing both the spatial distribution and the minimum required number of beacons to be determined under conservative sensor noise and process uncertainty assumptions representative of commercial off-the-shelf (COTS) hardware. The resulting formulation enables systematic design of physically realizable beacon layouts that maintain observability and estimation accuracy across realistic proximity operations scenarios in cislunar and deep-space environments.

The contributions of this paper are fourfold. First, we present a LOS-aware beacon-placement optimization framework for relative navigation around structurally complex spacecraft, explicitly accounting for geometric occlusions induced by spacecraft structures. Second, we introduce a CSP–DG formulation that enables gradient-based optimization of beacon locations constrained to a discrete set of structural rails, while provably converging to physically realizable, fully discrete solutions. Third, we develop a computationally efficient and numerically robust ellipsoidal occlusion model for LOS evaluation, based on a constrained-minimum test of ray–ellipsoid intersections, and integrate it directly into a CD–EKF with range measurements. Fourth, we formulate beacon placement as a robustness-driven design problem by optimizing the worst-case $P_{99}$ position error across a dense tube of realistic servicing trajectories derived from multiple fuel-optimal TR-CRTBP rendezvous solutions.

## SPACE TELESCOPE STRUCTURAL GEOMETRY AND RAIL LAYOUT

This section describes the geometry of the space telescope structure used throughout this work. A detailed CAD model of a conceptual large-aperture space telescope was previously developed by the authors in SolidWorks for use in attitude dynamics studies.[7] The same structure is adopted here, and is shown in Fig. 1a. The telescope consists of five sunshield blocks arranged in a cross-shaped configuration, each with dimensions $10 \times 10 \times 2$ m, a primary mirror of diameter 10 m, a light collector assembly, and a spacecraft bus located beneath the sunshield.[7] In the present study, the perimeter of the sunshield plays a direct role, as this is the region where navigation beacons may be physically mounted. These admissible mounting locations are highlighted as thick black lines along the sunshield edges in Fig. 1a. The remaining telescope geometry also plays an important role through the LOS occlusion analysis.

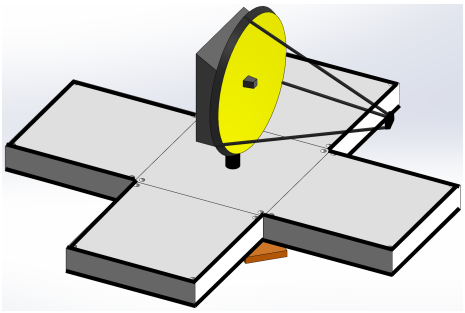

(a) CAD model of the conceptual space telescope. Navigation beacons may be installed along the thick black perimeter rails on the upper and lower faces of the sunshield.

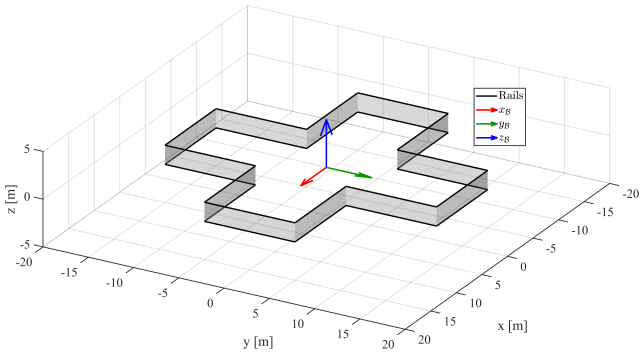


(b) Schematic of the discrete rail network on the sunshield. The 24 allowable beacon rails are shown as thick black segments, arranged in two layers at $z = +1$ and $z = -1$ m in the body frame $\mathcal{B}$.

**Figure 1**: Sunshield geometry and allowable beacon-mounting rails.

To clearly illustrate the discrete rail network used for beacon placement, Fig. 1b presents a schematic of the sunshield perimeter. For visualization, the outer faces of the sunshield blocks are lightly shaded, while the rails themselves are shown in thick black lines. All other components of the telescope are omitted to emphasize the rail layout and its geometric dimensions. The coordinate system used throughout this work is

the body frame $\mathcal{B}$, whose origin is located at the geometric center of the sunshield assembly. The $x_{\mathcal{B}}$ and $y_{\mathcal{B}}$ axes lie in the sunshield plane, while $z_{\mathcal{B}}$ is normal to the plane. The orientation and axes of this frame are illustrated in Fig. 1b. This frame is used to define all beacon positions, rail coordinates, reference trajectories, and the occlusion geometry used in the LOS visibility tests. The sunshield contains 24 distinct rails in total: 12 positioned on the upper surface and 12 directly beneath them on the lower surface, forming two parallel layers at $z = +1$ m and $z = -1$ m in the $\mathcal{B}$ frame. Each rail is a straight edge representing a rigid, mountable structural member. The full rail set forms a closed perimeter around the cross-shaped sunshield.

The structural dimensions and mass properties of this telescope concept were inspired by preliminary design parameters reported for the James Webb Space Telescope.[7,30] These references were used to ensure that the mass distribution and geometric scale of the CAD model are representative of a realistic large-aperture observatory. Nonetheless, the structure employed here is a simplified, research-oriented abstraction rather than an operational spacecraft design. Its purpose is to provide a realistic but tractable example of a complex, discrete geometry on which to demonstrate the proposed CSP–DG and LOS–aware beacon placement methodology.

## CONTINUOUS SURFACE PARAMETERIZATION FOR DISCRETE GEOMETRY

Navigation beacons must be mounted on a discrete set of structural rails that form the perimeter of the target spacecraft, as shown in Figs. 1a and 1b. Directly optimizing over this discrete surface leads to a highly non-convex problem and produces poor gradient behavior for continuous optimization methods. To address this challenge, we introduce a Continuous Surface Parameterization for Discrete Geometry (CSP–DG) formulation, which provides a smooth, differentiable representation of discrete geometries into a continuous optimization space. This parameterization allows the use of gradient-based solvers while still ensuring that the final optimized solutions lie on the underlying discrete geometry.

Let the target structure include $K$ distinct perimeter rails, indexed by $k = 1, \ldots, K$. Each rail is parameterized by a curve:

$$c_k : [0, 1] \to \mathbb{R}^3, \qquad u \mapsto c_k(u) \tag{1}$$

where $u \in [0, 1]$ is a normalized arc-length parameter. For the two-layer perimeter geometry used in this work, each rail is a straight line segment with fixed height $z = \pm 1$ in the $\mathcal{B}$ frame, and its parametrization is given by the linear interpolation:

$$c_k(u) = (1 - u)\, \mathbf{v}_0^k + u\, \mathbf{v}_1^k \tag{2}$$

where $\mathbf{v}_0^k, \mathbf{v}_1^k \in \mathbb{R}^3$ denote the endpoints of the $k^{\text{th}}$ rail. Let $N_b$ be the total number of beacons. For each beacon $i \in \{1, \ldots, N_b\}$, we introduce a continuous decision vector:

$$\mathbf{z}_i = \begin{bmatrix} \mathbf{a}_i \\ \mathbf{b}_i \end{bmatrix} \in \mathbb{R}^{2K} \tag{3}$$

where the vector $\mathbf{a}_i \in \mathbb{R}^K$ contains softmax logits that control how strongly beacon $i$ is associated with each rail, and $\mathbf{b}_i \in \mathbb{R}^K$ determines local coordinates along each rail. The logits $\mathbf{a}_i$ are converted into non-negative mixture weights through a softmax function:[31]

$$w_{ik} = \frac{\exp(a_{ik}/T_{\text{softmax}})}{\sum_{\ell=1}^{K} \exp(a_{i\ell}/T_{\text{softmax}})} \tag{4}$$

where the scalar $T_{\text{softmax}} > 0$ governs the sharpness of the distribution. Small values of $T_{\text{softmax}}$ amplify differences in logits and drive the distribution toward a nearly discrete, single-rail assignment. Larger values flatten the distribution, yielding a more diffuse mixture across the rails. Because exponentials magnify relative differences (i.e., $\exp(a_{11})$ becomes much larger than $\exp(a_{12})$ even if $a_{11}$ exceeds $a_{12}$ only slightly), the softmax serves as a smooth relaxation of a discrete selection mechanism. For every beacon, the weights satisfy:

$$w_{ik} \geq 0 \tag{5}$$

$$\sum_{k=1}^{K} w_{ik} = 1 \tag{6}$$

The vector $\mathbf{b}_i$ specifies local rail coordinates. Each entry is transformed to the interval $(0, 1)$ through the logistic sigmoid:

$$u_{ik} = \frac{1}{1 + \exp(-b_{ik})} \tag{7}$$

ensuring a valid position along each rail. Together, $(w_{ik}, u_{ik})$ encodes both which rails are emphasized and where on those rails the beacon lies.

Let $\mathbf{p}_i \in \mathbb{R}^3$ denote the position of beacon $i$. Using these quantities, the CSP–DG position of beacon $i$ is defined as:

$$\mathbf{p}_i = \sum_{k=1}^{K} w_{ik}\, c_k(u_{ik}) \tag{8}$$

Since each $c_k(\cdot)$ is smooth and both $w_{ik}$ and $u_{ik}$ are smooth functions of $a_{ik}$ and $b_{ik}$, the mapping $\mathbf{z}_i \mapsto \mathbf{p}_i$ is differentiable. This enables efficient use of gradient-based optimization without the need for discrete combinatorial search.

Mixture models may yield ambiguous or overly diffuse rail associations. To bias the optimizer toward discrete rail assignments and to penalize uncertainty in the softmax distribution, two regularization functions are introduced. The first is the Shannon entropy which is widely used in information theory:[32]

$$H_i = -\sum_{k=1}^{K} w_{ik} \log w_{ik} \tag{9}$$

which satisfies $0 \leq H_i \leq \log K$ and quantifies the dispersion of the weight vector. Entropy is minimized when the distribution is concentrated on a single rail ($H_i = 0$) and maximized when the weights are uniform. The second is the quadratic diffusiveness measure or the Gini impurity:[33]

$$D_i = 1 - \sum_{k=1}^{K} w_{ik}^2 \tag{10}$$

which attains its minimum $D_i = 0$ under a perfectly discrete distribution and increases monotonically as the distribution becomes more diffuse. Together, these two quantities provide complementary measures of concentration and form the aggregate regularization cost:

$$J_{\text{reg}} = \eta_{\text{ent}} \sum_{i=1}^{N_b} H_i + \eta_{\text{diffuse}} \sum_{i=1}^{N_b} D_i \tag{11}$$

where $\eta_{\text{ent}} > 0$ and $\eta_{\text{diffuse}} > 0$ control the strength of the penalties. Their role is to smoothly steer the optimization toward low-entropy, single-rail solutions while preserving differentiability throughout the search. Collecting all variables, the full CSP–DG decision vector is defined as:

$$\mathbf{z} = \begin{bmatrix} \mathbf{z}_1 \\ \vdots \\ \mathbf{z}_{N_b} \end{bmatrix} \in \mathbb{R}^{2KN_b} \tag{12}$$

with associated hyperparameters:

- $T_{\text{softmax}}$ controlling the sharpness of rail selection,
- $\eta_{\text{ent}}$ weighting the entropy penalty, and

- $\eta_{\text{diffuse}}$ weighting the diffusiveness penalty.

This fully defines the CSP–DG formulation and determines how strongly the optimizer pushes towards discrete rail assignments while maintaining differentiability throughout the search process.

The beacon-placement problem is posed as a continuous nonlinear optimization over the defined CSP–DG decision vector $\mathbf{z} \in \mathbb{R}^{2KN_b}$. Each candidate $\mathbf{z}$ is decoded into a set of continuous beacon positions:

$$\mathbf{P}(\mathbf{z}) = \big[\mathbf{p}_1(\mathbf{z}) \ \cdots \ \mathbf{p}_{N_b}(\mathbf{z})\big] \in \mathbb{R}^{3\times N_b} \tag{13}$$

where $\mathbf{p}_i(\mathbf{z})$ is given by the CSP–DG representation in Eq. (8).

## ELLIPSOIDAL OCCLUSION MODEL FOR LINE-OF-SIGHT CONSTRAINTS

The sunshield and primary mirror of the telescope are large, opaque structures that partially obstruct the line of sight (LOS) between the servicing spacecrafts and the perimeter rails on which the beacons are mounted. To incorporate these occlusions in a way that is both geometrically accurate and computationally tractable, the physical geometry is approximated by a union of convex ellipsoids. This ellipsoidal model is used solely for LOS evaluation; the CSP–DG rail parameterization and beacon-placement optimization remain unchanged.

### Ellipsoidal approximation of the sunshield and mirror

Two orthogonal sunshield arms and the primary mirror are each represented by an axis-aligned ellipsoid in the $\mathcal{B}$ frame. For ellipsoid $j \in \{1, 2, 3\}$, let $\mathbf{c}_j \in \mathbb{R}^3$ denote its center and let:

$$\mathbf{e}_j = \begin{bmatrix} e_{jx} \\ e_{jy} \\ e_{jz} \end{bmatrix}$$

denote its semi-axes along the $x$, $y$, and $z$ directions, respectively. The corresponding quadratic-form matrix is:

$$\mathbf{E}_j = \operatorname{diag}\left(\frac{1}{e_{jx}^2}, \frac{1}{e_{jy}^2}, \frac{1}{e_{jz}^2}\right) \tag{14}$$

The implicit equation of ellipsoid $j$ is then:[34]

$$\Phi_j(\mathbf{x}) = \big(\mathbf{x} - \mathbf{c}_j\big)^\top \mathbf{E}_j \big(\mathbf{x} - \mathbf{c}_j\big) - 1 = 0 \tag{15}$$

with the interior, boundary, and exterior regions given by:

$$\Phi_j(\mathbf{x}) < 0 \ \ \text{(interior)}, \qquad \Phi_j(\mathbf{x}) = 0 \ \ \text{(surface)}, \qquad \Phi_j(\mathbf{x}) > 0 \ \ \text{(exterior)} \tag{16}$$

Figure 2 shows the ellipsoidal approximation of the space telescope. In this work, the two sunshield arms are modeled as elongated ellipsoids centered at the origin and extended along the $\pm x_{\mathcal{B}}$ and $\pm y_{\mathcal{B}}$ directions, with in-plane dimensions of approximately $30 \times 10\,\text{m}$ and thickness $4\,\text{m}$ along $z_{\mathcal{B}}$. The primary mirror is represented as a thin ellipsoid whose cross-section in the $y$–$z$ plane is a circle of diameter $10\,\text{m}$, with a small thickness along $x_{\mathcal{B}}$ and its center located above the sunshield plane at $z_{\mathcal{B}} \approx 6\,\text{m}$. These parameters are chosen so that the ellipsoids tightly enclose the CAD geometry of the sunshield panels and mirror, while remaining smooth and convex.

By construction, the rails used for beacon placement lie strictly outside the ellipsoids. That is, for any admissible beacon position $\mathbf{p}_i$ on the perimeter rails:

$$\Phi_j(\mathbf{p}_i) \geq 0, \qquad \forall j \tag{17}$$

Similarly, the trajectories of the servicing spacecrafts are designed to evolve in the exterior region of the occluders. The ellipsoids therefore act as opaque volumetric obstacles: their interiors are never admissible for either the trajectories or the beacons, and they block optical paths that intersect $\Phi_j(\mathbf{x}) < 0$.

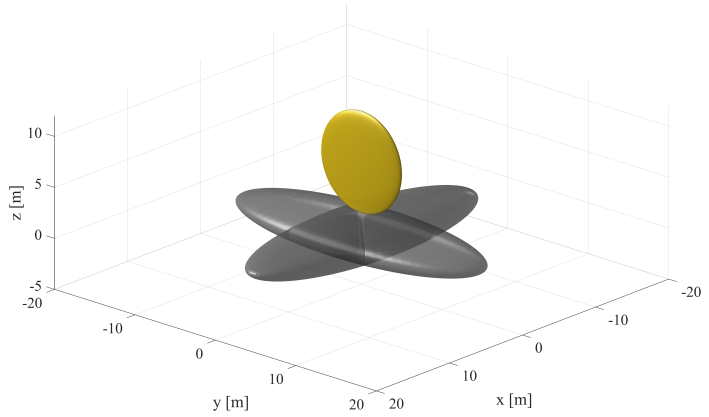


**Figure 2**: Ellipsoidal approximation of the telescope's sunshield and primary mirror.

This ellipsoidal approximation is particularly well suited to the present problem for two reasons. First, it provides a compact and differentiable representation of large structural elements whose detailed CAD geometry would otherwise require expensive mesh-based ray tracing. Second, the intersection of a straight LOS segment with a quadratic surface admits a closed-form algebraic characterization, which makes LOS checks both efficient and numerically robust across many trajectories and beacon layouts.

**Ray–ellipsoid intersection for LOS evaluation**

Consider the line segment connecting the true servicing spacecarft position $\mathbf{o} \in \mathbb{R}^3$ at time $t$ and a candidate beacon position $\mathbf{p}_i \in \mathbb{R}^3$ in the body frame. Let:

$$\mathbf{u} = \frac{\mathbf{p}_i - \mathbf{o}}{\|\mathbf{p}_i - \mathbf{o}\|}, \qquad L = \|\mathbf{p}_i - \mathbf{o}\| \tag{18}$$

denote the unit direction vector from the spacecraft to the beacon and the segment length, respectively.[34] A point along the segment is parameterized as:

$$\mathbf{x}(s) = \mathbf{o} + s\,\mathbf{u}, \qquad s \in [0,\, L] \tag{19}$$

where $s = 0$ corresponds to the servicing spacecraft and $s = L$ to the beacon. Substituting the ray parameterization of Eq. (19) into the implicit ellipsoid equation of Eq. (15) for ellipsoid $j$ yields a scalar quadratic in $s$:

$$\begin{aligned} f_j(s) &= \Phi_j\big(\mathbf{x}(s)\big) = \big(\mathbf{o} + s\mathbf{u} - \mathbf{c}_j\big)^\top \mathbf{E}_j \big(\mathbf{o} + s\mathbf{u} - \mathbf{c}_j\big) - 1 \\ &= \alpha_j s^2 + 2\beta_j s + \gamma_j \end{aligned} \tag{20}$$

with coefficients:

$$\alpha_j = \mathbf{u}^\top \mathbf{E}_j \mathbf{u}, \qquad \beta_j = (\mathbf{o} - \mathbf{c}_j)^\top \mathbf{E}_j \mathbf{u}, \qquad \gamma_j = (\mathbf{o} - \mathbf{c}_j)^\top \mathbf{E}_j (\mathbf{o} - \mathbf{c}_j) - 1 \tag{21}$$

Because $\mathbf{E}_j$ is positive definite, $\alpha_j > 0$ for any nonzero direction $\mathbf{u}$, and $f_j(s)$ is strictly convex in $s$. For an infinite line, the standard intersection criterion is based on the discriminant of Eq. (20):

$$\Delta_j = (2\beta_j)^2 - 4\alpha_j\gamma_j \tag{22}$$

The three classical cases are:[34]

- $\Delta_j < 0$: no real roots, so the line misses the ellipsoid.

- $\Delta_j = 0$: a single repeated root, corresponding to a tangent intersection.
- $\Delta_j > 0$: two distinct real roots, corresponding to an entry and an exit point.

However, the LOS problem is concerned with a finite segment $s \in [0, L]$, not the infinite line. Even if the infinite line intersects the ellipsoid, the intersection is only relevant for occlusion if at least one of the real roots $s_{j,1}$, $s_{j,2}$ produced by Eq. (20) lies in the interval $[0, L]$. Intuitively, the ray "may" intersect the ellipsoid somewhere, but the intersection matters for LOS only when it occurs between the spacecraft and the beacon.

A direct discriminant-based implementation can be numerically fragile for thin, highly anisotropic ellipsoids. When one semi-axis is much larger or smaller than the others, the entries of $\mathbf{E}_j$ span several orders of magnitude. In such cases, the constant term $\gamma_j$ and the discriminant $\Delta_j$ can suffer from severe cancellation in floating-point arithmetic, and the classification $\Delta_j \lesseqgtr 0$ becomes ill-conditioned.

**Constrained minimum test and numerical robustness**

To avoid these conditioning issues, the LOS algorithm in this work evaluates the minimum value of $f_j(s)$ along the finite segment rather than relying solely on the discriminant. The minimum of $f_j(s)$ on the real line occurs at:

$$\frac{d\, f_j(s)}{d\, s} = 0 \tag{23}$$

Solving for $s_j$ gives:

$$s^* = -\frac{\beta_j}{\alpha_j} \tag{24}$$

and the corresponding minimum value is:

$$f_{j,\min} = f_j(s^*) = \alpha_j \left(s^*\right)^2 + 2\beta_j s^* + \gamma_j \tag{25}$$

The LOS between the servicing spacecraft and beacon $i$ is declared blocked by ellipsoid $j$ if the ray penetrates the interior of the ellipsoid at some point strictly between the endpoints. This occurs when:

$$\bar{f}_{j,\min} < 0 \tag{26}$$

In practice, a small scale-aware tolerance is applied and the condition is implemented as:

$$\bar{f}_{j,\min} \leq -\varepsilon_j, \qquad \varepsilon_j = \varepsilon_{\text{scale}} \max\{1,\, |\Phi_j(\mathbf{o})|\} \tag{27}$$

to provide robustness against roundoff error. If this inequality holds for any ellipsoid in the set, the LOS to beacon $i$ is considered occluded:

$$\exists j \text{ such that } \bar{f}_{j,\min} \leq -\varepsilon_j \quad \Rightarrow \quad \text{LOS to beacon } i \text{ is blocked} \tag{28}$$

Conversely, if $\bar{f}_{j,\min} > 0$ for all $j$, the entire segment from the spacecraft to beacon $i$ remains in the exterior of every ellipsoid and the LOS is clear.

**Illustrative LOS Scenarios**

To illustrate the behavior of the ellipsoidal occlusion model, we consider a simple configuration with a single beacon and three viewpoint locations. As shown in Fig. 3, the beacon is placed on the top surface of the $x_{\mathcal{B}}$-aligned sunshield ellipsoid. Three viewpoint positions $\mathbf{o}_1, \mathbf{o}_2, \mathbf{o}_3$ are then selected such that the corresponding LOS segments result in distinct geometric cases. The three viewpoint locations $\mathbf{o}_1, \mathbf{o}_2, \mathbf{o}_3$ may be interpreted as instantaneous positions of the servicing spacecrafts along their approach trajectories.

Figure 3 shows the ellipsoidal approximation of the sunshield and mirror together with the beacon and the three viewpoints. The red segments correspond to LOS paths that are classified as blocked by the constrained minimum test on $f_j(s)$, whereas the green segment corresponds to a clear LOS. Specifically:

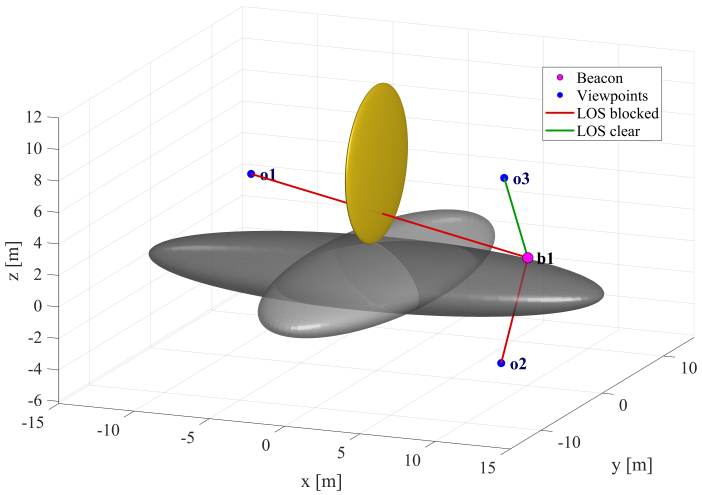


**Figure 3**: Example LOS configurations for one beacon and three viewpoints using the ellipsoidal approximation of the sunshield and primary mirror.

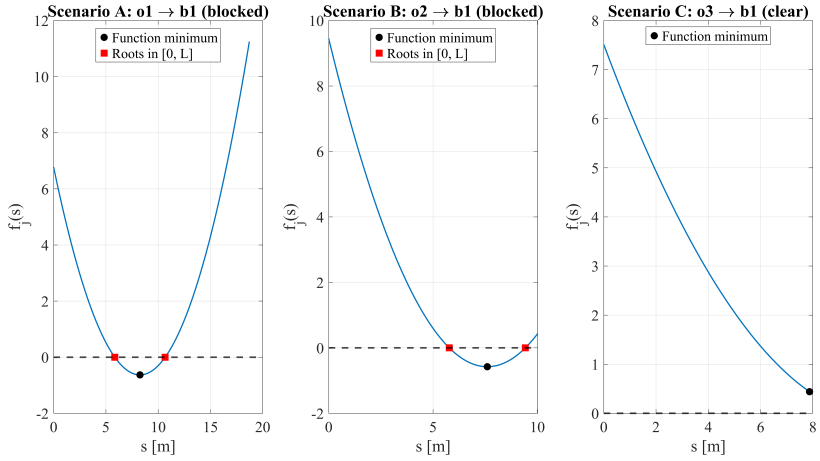


**Figure 4**: Quadratic profiles $f_j(s)$ for the three LOS scenarios in Fig. 3.

- **Scenario A** ($\mathbf{o}_1 \rightarrow \mathbf{b}_1$): the ray intersects the mirror ellipsoid, producing two real roots corresponding to the entry and exit points of the segment through the ellipsoid.
- **Scenario B** ($\mathbf{o}_2 \rightarrow \mathbf{b}_1$): the ray similarly intersects the sunshield ellipsoid beneath the beacon, again producing two real roots associated with the entry and exit points of the ray through the ellipsoid.
- **Scenario C** ($\mathbf{o}_3 \rightarrow \mathbf{b}_1$): the ray remains in the exterior of all ellipsoids and is therefore classified as clear.

For each scenario, Fig. 4 plots the scalar quadratic $f_j(s)$ in Eq. (20) associated with the most critical ellipsoid $j^*$, i.e., the ellipsoid that attains the smallest constrained minimum along $s \in [0, L]$. In Scenarios A and B, $f_{j^*}(s)$ has two real roots in $[0, L]$ and a negative constrained minimum, indicating that the LOS segment penetrates the interior of the ellipsoid and is thus blocked. In Scenario C, $f_{j^*}(s)$ remains strictly positive over $[0, L]$, so the LOS is unobstructed. These examples highlight how the quadratic profile $f_j(s)$ provides a simple and numerically robust diagnostic for LOS classification under the ellipsoidal occlusion model.

These three cases represent a few of the limited LOS outcomes that can occur under the modeling assumptions that all beacons are constrained to lie strictly on the exterior surface of the ellipsoidal occluders (i.e., on the perimeter rails). If a beacon were placed inside an ellipsoid, the ray would originate outside and terminate inside the interior region, guaranteeing an occlusion regardless of the servicing spacecraft position. Such configurations are therefore excluded.

**Integration with beacon placement and EKF evaluation**

At each time step along each trajectory, the ellipsoidal occlusion model is used to construct a LOS visibility test for the current beacon layout. Let $\mathbf{r}_{\mathrm{true}}(t_{\mathcal{K}})$ denote the true servicing spacecraft position. For each beacon $i$, the ray–ellipsoid test described above is applied with $\mathbf{o} = \mathbf{r}_{\mathrm{true}}(t_{\mathcal{K}})$ and $\mathbf{p}_i$, yielding a binary outcome: either the beacon is visible (no ellipsoid intersection) or occluded (at least one ellipsoid intersection). The set of visible beacons at time $t$ is denoted by

$$\mathcal{V}_{\mathcal{K}}(\mathbf{z}) \subseteq \{1, \ldots, N_b\} \tag{29}$$

This visibility set enters the state-estimation problem through the range measurement model: only beacons in $\mathcal{V}_{\mathcal{K}}(\mathbf{z})$ contribute measurements to the EKF at time $t_{\mathcal{K}}$, while occluded beacons are simply omitted. Importantly, the formulation does not require every beacon to be visible at every time step. Instead, the objective function evaluates the EKF performance across the entire ensemble of trajectories using the time-varying visibility pattern induced by the ellipsoidal occluders. Beacon layouts that concentrate beacons in regions that are frequently shadowed by the sunshield or mirror tend to yield poor observability and large estimation errors, whereas layouts that maintain a well-distributed set of visible beacons along typical servicing trajectories achieve significant robustness.

In this way, LOS constraints are implicitly enforced within the beacon-placement optimization through the occlusion-aware EKF evaluation, rather than through explicit visibility constraints. Beacon layouts that lead to frequent self-occlusions naturally result in degraded measurement availability, poorer observability, and larger estimation errors, which are directly reflected in an increased value of the objective function. Conversely, layouts whose CSP–DG rail locations remain visible for a substantial portion of the trajectory ensemble yield improved EKF performance and are automatically favored by the optimizer. This formulation tightly couples the physical telescope geometry, LOS visibility, and estimation performance, allowing realistic LOS effects to be incorporated in a fully continuous and differentiable optimization framework.

## MINIMUM-SEPARATION DISTANCE CONSTRAINT

A physically realistic beacon layout must prevent two beacons from being placed arbitrarily close to one another on the spacecraft structure. Such clustering is undesirable for several reasons: it leads to redundant geometry in the range measurement model, reduces the spatial diversity required for good observability, and violates practical mechanical mounting constraints on large spacecraft surfaces. To ensure geometric diversity and physical realizability, a minimum-separation constraint is imposed between all beacon locations.

Let us define $d_{\min} > 0$ as the required minimum Euclidean distance between any two beacons. For every beacon pair $(i, l)$, the separation constraint is written as:

$$\left\|\mathbf{p}_i - \mathbf{p}_l\right\| \;\geq\; d_{\min}, \qquad 1 \leq i < l \leq N_b \tag{30}$$

Equivalently, this may be expressed in squared-distance form as a set of nonlinear inequality constraints:

$$g_{il}(\mathbf{z}) = d_{\min}^2 - \left\|\mathbf{p}_i(\mathbf{z}) - \mathbf{p}_l(\mathbf{z})\right\|^2 \;\leq\; 0 \tag{31}$$

The constraint in Eq. (30) ensures that every pair of beacons maintains a minimum physical and geometric spacing on the rail structure. In this work, a minimum beacon–to–beacon spacing of $d_{\min} = 5$ m is imposed. This promotes well-conditioned range measurements, prevents degenerate configurations that harm EKF observability, and enforces a realistic installation footprint for the beacon hardware.

## TRAJECTORY SET CONSTRUCTION

The evaluation of any beacon-placement strategy must be performed across a representative ensemble of servicing trajectories that capture both the nominal motion of the servicing spacecraft and realistic variations around it. To this end, a two-stage approach is adopted. First, we import four fuel-optimal reference trajectories that were previously generated using a TR-CRTBP dynamical model.[5] These trajectories serve as high-fidelity nominal and fuel-optimal paths representative of servicing operations near the Sun–Earth $L_2$ point. Second, a larger set of smooth perturbed trajectories is synthesized around these reference solutions to capture the range of motions expected during proximity operations and to ensure robustness of the EKF to variations in translational motion.

### Reference Trajectories from Target-Relative CRTBP Dynamics

The four reference trajectories used in this work originate from a high-fidelity TR-CRTBP dynamical model developed in our previous publication.[5] This model reformulates the Sun–Earth CRTBP into a numerically well-conditioned, target-relative representation suitable for modeling proximity operations near the $L_2$ point. In brief, the standard CRTBP is shifted so that the origin is located at the Sun–Earth $L_2$ point, and the distance unit is rescaled using a scaling factor to ensure that relative motion remains numerically well behaved.[5] This transformation preserves the structure of the CRTBP equations but eliminates numerical stiffness caused by the disparity between the interplanetary length scales and the small relative distances encountered during spacecraft proximity operations. Under this shifted and rescaled model, four fuel-optimal rendezvous trajectories were computed using an indirect optimal control formulation.[5] These solutions represent dynamically consistent approach trajectories that capture the nonlinear dynamics of the Sun–Earth $L_2$ Halo orbit.

Because the focus of the present paper is on beacon placement and state estimation rather than trajectory optimization, the details of the dynamical model, scaling, and optimal control formulation are omitted here. A full derivation of the TR-CRTBP formulation and the methodology used to generate the four optimal trajectories may be found in our prior journal publication.[5]

### Perturbed Trajectory Tube Generation

Let $\mathbf{x}_{\mathrm{ref}}(t) \in \mathbb{R}^6$ denote the target-relative state history of one of the four reference trajectories, and let $\mathbf{a}_{\mathrm{ref}}(t) \in \mathbb{R}^3$ denote its corresponding acceleration or thrust history. A synthetic trajectory is constructed by applying constant spatial and velocity offsets:

$$\mathbf{x}_{\mathrm{syn}}(t) = \mathbf{x}_{\mathrm{ref}}(t) + \begin{bmatrix} \Delta\mathbf{x} \\ \Delta\dot{\mathbf{x}} \end{bmatrix} \tag{32}$$

where $\Delta\mathbf{x}, \Delta\dot{\mathbf{x}} \in \mathbb{R}^3$ are sampled from zero-mean Gaussian distributions with user-specified standard deviations. The acceleration history is retained as:

$$\mathbf{a}_{\mathrm{syn}}(t) = \mathbf{a}_{\mathrm{ref}}(t) \tag{33}$$

so that only the translational motion is perturbed while the underlying thrust profile remains physically consistent. These offsets remain fixed along the entire trajectory to ensure smoothness and to avoid introducing artificial acceleration discontinuities. A total of $N_{\mathrm{syn}}$ synthetic trajectories are created by randomly selecting which reference trajectory to perturb. Figure 5 illustrates the four fuel-optimal reference trajectories from Ref. 5, together with a dense tube of 96 additional perturbed trajectories generated for this study. The resulting ensemble forms a "trajectory tube" around the nominal paths and effectively captures expected operational variability in initial conditions and approach geometries. The full space telescope geometry is omitted from Fig. 5 to avoid visual clutter; instead, the telescope center is indicated by a black star.

It is noted that the resulting synthetic trajectories are not strictly dynamically feasible, in the sense that the retained acceleration history $\mathbf{a}_{\mathrm{ref}}(t)$ does not exactly satisfy the equations of motion for the offset state

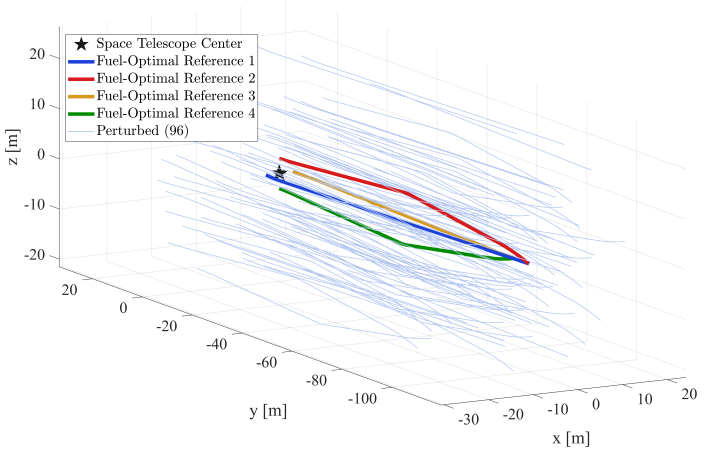


**Figure 5**: Four fuel-optimal reference trajectories (bold) and 96 offset trajectories forming the evaluation tube used for state-estimation robustness analysis.

$\mathbf{x}_{\text{syn}}(t)$. Consequently, the perturbed trajectories are not exact solutions of the TR-CRTBP dynamics. However, for the purposes of beacon-placement and state-estimation analysis, these trajectories may be regarded as near-consistent. The imposed offsets are small relative to the characteristic length and velocity scales of the Sun–Earth $L_2$ vicinity, and the target-relative dynamics in this region are locally near-linear.[5] The perturbed trajectory tube should be interpreted as a representative sampling of relative states encountered during proximity operations rather than as a set of executable guidance solutions.

### Trajectory Set Assembly and Subsampling

The complete data set is formed by combining the four reference trajectories with the $N_{\text{syn}}$ synthesized members:

$$\mathcal{T} = \{\mathcal{T}_1, \ldots, \mathcal{T}_4\} \cup \{\mathcal{T}_{\text{syn},1}, \ldots, \mathcal{T}_{\text{syn},N_{\text{syn}}}\} \tag{34}$$

Each trajectory consists of a time history $\{t\}$, a relative state history $\{\mathbf{x}(t)\}$, and an associated acceleration or input history $\{\mathbf{a}(t)\}$. For use within the beacon-placement optimization and the LOS-aware EKF, each trajectory is uniformly subsampled. Let a trajectory contain $n_{samples}$ samples and let $M_{\text{eval}}$ be the desired number of evaluation points. We define the stratified sampling indices as:

$$\kappa_\chi = \left\lfloor 1 + (\chi - 1)\frac{n_{samples} - 1}{M_{\text{eval}} - 1} \right\rfloor, \qquad \chi = 1, \ldots, M_{\text{eval}} \tag{35}$$

which preserves the endpoints and ensures uniform spacing across the arc length of the trajectory. This procedure reduces computational cost while maintaining the essential geometric and dynamical features needed for EKF performance assessment. The final trajectory set supplied to the optimization therefore contains:

$$N_{\text{traj}} = 4 + N_{\text{syn}} \tag{36}$$

members, each subsampled to $M_{\text{eval}}$ points. This ensemble provides sufficient variability to ensure that any beacon configuration performing well across these trajectories is robust to realistic operational perturbations and wide range of approach trajectories.

## STATE ESTIMATION USING A CONTINUOUS–DISCRETE EXTENDED KALMAN FILTER

Accurate evaluation of any beacon layout requires a consistent state-estimation framework capable of processing range measurements from the selected beacon configuration. In this work, state estimation is performed using a CD–EKF, which models the translational dynamics continuously while incorporating discrete

range measurements at the sampling instants of the trajectory set.[10] A continuous–discrete EKF is the appropriate choice for this study because the relative translational motion of the servicing spacecraft evolves continuously in time, whereas range measurements from the beacons are available only at discrete sampling instants. This hybrid filtering structure accurately reflects the physical sensing architecture and avoids the modeling errors that arise when discretizing dynamics or artificially modifying the measurement rate. Additionally, the CD–EKF naturally accommodates the constant velocity (CV(2)) process model and variable time steps present in the trajectory set, making it more numerically stable and representative of practical onboard estimation compared to a purely discrete EKF formulated at fixed sampling intervals.[10]

The EKF estimates the relative translational state of the servicing spacecraft:

$$\boldsymbol{\xi}(t) = \begin{bmatrix} \mathbf{r}(t) \\ \mathbf{v}(t) \end{bmatrix} \in \mathbb{R}^6 \tag{37}$$

where $\mathbf{r}(t) \in \mathbb{R}^3$ is the relative position and $\mathbf{v}(t) \in \mathbb{R}^3$ is the relative velocity in the $\mathcal{B}$ frame. The servicing spacecraft is modeled with a constant-velocity (CV(2)) kinematic model driven by zero-mean white acceleration noise:[10]

$$\dot{\boldsymbol{\xi}}(t) = \mathbf{F}_c\, \boldsymbol{\xi}(t) + \mathbf{G}\, \mathbf{w}(t), \qquad \mathbf{w}(t) \sim \mathcal{N}\big(\mathbf{0},\, q_a \mathbf{I}_3\big) \tag{38}$$

with:

$$\mathbf{F}_c = \begin{bmatrix} \mathbf{0}_{3\times3} & \mathbf{I}_3 \\ \mathbf{0}_{3\times3} & \mathbf{0}_{3\times3} \end{bmatrix}, \qquad \mathbf{G} = \begin{bmatrix} \mathbf{0}_{3\times3} \\ \mathbf{I}_3 \end{bmatrix} \tag{39}$$

where $q_a > 0$ is the (scalar) white-acceleration spectral density and $\mathbf{I}_3$ is the $3 \times 3$ identity matrix. The CV(2) model is a deliberately simplified kinematic model that treats the relative motion as constant-velocity driven by white acceleration noise. This abstraction is intentional: the purpose of the robustness study is to isolate the effect of beacon geometry and LOS occlusions on estimation performance, without giving the EKF an overly informative or problem-specific dynamical model. The true trajectories still evolve according to full nonlinear dynamics, but the filter only uses a minimal kinematic predictor to stress-test performance under sparse, range-only measurements.

Let the trajectories be sampled at times $t_{\mathcal{K}}$ with variable step $\Delta t_{\mathcal{K}} = t_{\mathcal{K}} - t_{\mathcal{K}-1}$. The continuous CV(2) model admits a closed-form discretization, yielding the state-transition matrix:

$$\mathbf{F}_d(\Delta t_{\mathcal{K}}) = \begin{bmatrix} \mathbf{I}_3 & \Delta t_{\mathcal{K}}\, \mathbf{I}_3 \\ \mathbf{0}_{3\times3} & \mathbf{I}_3 \end{bmatrix} \tag{40}$$

and the corresponding discrete-time process-noise covariance:

$$\mathbf{Q}_d(\Delta t_{\mathcal{K}}) = q_a \begin{bmatrix} \dfrac{\Delta t_{\mathcal{K}}^3}{3}\, \mathbf{I}_3 & \dfrac{\Delta t_{\mathcal{K}}^2}{2}\, \mathbf{I}_3 \\ \dfrac{\Delta t_{\mathcal{K}}^2}{2}\, \mathbf{I}_3 & \Delta t_{\mathcal{K}}\, \mathbf{I}_3 \end{bmatrix} \tag{41}$$

At each step $\mathcal{K} \geq 1$, the EKF prediction (propagation) step is:[10]

$$\boldsymbol{\xi}_{\mathcal{K}}^{-} = \mathbf{F}_d(\Delta t_{\mathcal{K}})\, \boldsymbol{\xi}_{\mathcal{K}-1}^{+} \tag{42}$$

$$\mathbf{P}_{\mathcal{K}}^{-} = \mathbf{F}_d(\Delta t_{\mathcal{K}})\, \mathbf{P}_{\mathcal{K}-1}^{+} \mathbf{F}_d^{\top}(\Delta t_{\mathcal{K}}) + \mathbf{Q}_d(\Delta t_{\mathcal{K}}) \tag{43}$$

where $\mathbf{P}_{\mathcal{K}}$ denotes the state-estimation error covariance, and the superscripts $(\cdot)^-$ and $(\cdot)^+$ denote a priori (predicted) and a posteriori (updated) quantities, respectively.[10] At each sampling instant $t_{\mathcal{K}}$, the servicing spacecraft receives range measurements from all beacons that are visible, i.e., for which the LOS from the true spacecraft position to the beacon is not blocked by any ellipsoidal occluder. Let $\mathbf{r}_{\mathcal{K}}^{-}$ be the position component of $\boldsymbol{\xi}_{\mathcal{K}}^{-}$. The predicted noiseless range to beacon $i$ based on the current state estimate is:

$$h_i(\boldsymbol{\xi}_{\mathcal{K}}^{-}) = \big\|\mathbf{r}_{\mathcal{K}}^{-} - \mathbf{p}_i\big\| \tag{44}$$

LOS visibility, however, is determined using the true spacecraft position $\mathbf{r}_{\text{true}}(t_{\mathcal{K}})$: if the line segment connecting $\mathbf{r}_{\text{true}}(t_{\mathcal{K}})$ and $\mathbf{p}_i$ intersects any ellipsoid, beacon $i$ is deemed occluded and excluded from the measurement set. This reflects a physically realistic sensor model in which occlusion is governed by the true geometry rather than by the current EKF estimate. If all beacons are occluded at time $t_{\mathcal{K}}$, the EKF performs a pure prediction step with no update.

For the subset of visible beacons indexed by $\mathcal{V}_{\mathcal{K}}$, the stacked measurement model is:

$$\mathbf{y}_{\mathcal{K}} = \big[h_i(\boldsymbol{\xi}_{\mathcal{K}}^-)\big]_{i\,\in\,\mathcal{V}_{\mathcal{K}}} + \boldsymbol{\nu}_{\mathcal{K}}, \qquad \boldsymbol{\nu}_{\mathcal{K}} \sim \mathcal{N}\big(\mathbf{0},\, \sigma_r^2 \mathbf{I}_{n_{\mathcal{K}}}\big) \tag{45}$$

where $\sigma_r > 0$ is the range-measurement noise standard deviation, $\mathbf{I}_{n_{\mathcal{K}}}$ is the identity matrix of dimension $n_{\mathcal{K}} = |\mathcal{V}_{\mathcal{K}}|$, and $\boldsymbol{\nu}_{\mathcal{K}}$ is the measurement noise vector. The Jacobian of the scalar range measurement from beacon $i$ with respect to the EKF state is:

$$\mathbf{H}_{i,\mathcal{K}} = \frac{\partial h_i}{\partial \boldsymbol{\xi}}\bigg|_{\boldsymbol{\xi}_{\mathcal{K}}^-} = \begin{bmatrix} \dfrac{(\mathbf{r}_{\mathcal{K}}^- - \mathbf{p}_i)^\top}{\|\mathbf{r}_{\mathcal{K}}^- - \mathbf{p}_i\|} & \mathbf{0}_{1\times 3} \end{bmatrix} \tag{46}$$

and stacking the rows for all visible beacons yields the measurement matrix $\mathbf{H}_{\mathcal{K}} \in \mathbb{R}^{n_{\mathcal{K}}\times 6}$. The EKF update follows the standard continuous–discrete formulation. The innovation (residual) is:[10]

$$\tilde{\boldsymbol{y}}_{\mathcal{K}} = \mathbf{y}_{\mathcal{K}} - \mathbf{h}(\boldsymbol{\xi}_{\mathcal{K}}^-), \qquad \mathbf{h}(\boldsymbol{\xi}_{\mathcal{K}}^-) = \big[h_i(\boldsymbol{\xi}_{\mathcal{K}}^-)\big]_{i\,\in\,\mathcal{V}_{\mathcal{K}}} \tag{47}$$

and the innovation covariance is:[10]

$$\mathbf{S}_{\mathcal{K}} = \mathbf{H}_{\mathcal{K}} \mathbf{P}_{\mathcal{K}}^- \mathbf{H}_{\mathcal{K}}^\top + \sigma_r^2 \mathbf{I}_{n_{\mathcal{K}}} \tag{48}$$

To ensure numerical robustness, $\mathbf{S}_{\mathcal{K}}$ is symmetrized and augmented with a small positive diagonal "jitter" before inversion:

$$\mathbf{S}_{\mathcal{K}} \leftarrow \frac{\mathbf{S}_{\mathcal{K}} + \mathbf{S}_{\mathcal{K}}^\top}{2} + \varepsilon_s \mathbf{I}_{n_{\mathcal{K}}} \tag{49}$$

with $\varepsilon_s$ chosen on the order of $10^{-8}$. The Kalman gain is then:[10]

$$\mathbf{K}_{\mathcal{K}} = \mathbf{P}_{\mathcal{K}}^- \mathbf{H}_{\mathcal{K}}^\top \mathbf{S}_{\mathcal{K}}^{-1} \tag{50}$$

and the state and covariance updates are:[10]

$$\boldsymbol{\xi}_{\mathcal{K}}^+ = \boldsymbol{\xi}_{\mathcal{K}}^- + \mathbf{K}_{\mathcal{K}}\, \tilde{\boldsymbol{y}}_{\mathcal{K}} \tag{51}$$

$$\mathbf{P}_{\mathcal{K}}^+ = \big(\mathbf{I}_6 - \mathbf{K}_{\mathcal{K}}\mathbf{H}_{\mathcal{K}}\big)\mathbf{P}_{\mathcal{K}}^-\big(\mathbf{I}_6 - \mathbf{K}_{\mathcal{K}}\mathbf{H}_{\mathcal{K}}\big)^\top + \mathbf{K}_{\mathcal{K}}\sigma_r^2\mathbf{I}_{n_{\mathcal{K}}}\mathbf{K}_{\mathcal{K}}^\top \tag{52}$$

where $\mathbf{I}_6$ is the $6 \times 6$ identity matrix. Equation (52) is the Joseph-form covariance update, which guarantees symmetry and preserves positive definiteness even in the presence of roundoff errors. To avoid artificially optimistic performance, the EKF is deliberately initialized away from the true initial state using fixed position and velocity biases:

$$\boldsymbol{\xi}_0^+ = \boldsymbol{\xi}_{\text{true}}(t_0) + \begin{bmatrix} \Delta\mathbf{r}_0 \\ \Delta\mathbf{v}_0 \end{bmatrix} \tag{53}$$

where $\Delta\mathbf{r}_0, \Delta\mathbf{v}_0 \in \mathbb{R}^3$ are small constant offsets at $t_0$. The initial covariance $\mathbf{P}_0$ is chosen to reflect moderate uncertainty in both position and velocity, consistent with these biases. At each subsequent time step, the EKF executes either a full predict–update cycle (if at least one beacon is visible) or a prediction-only step (if all beacons are occluded). After every step, the instantaneous position and velocity errors:

$$e_{r,\mathcal{K}} = \big\|\mathbf{r}_{\mathcal{K}}^+ - \mathbf{r}_{\text{true}}(t_{\mathcal{K}})\big\|, \qquad e_{v,\mathcal{K}} = \big\|\mathbf{v}_{\mathcal{K}}^+ - \mathbf{v}_{\text{true}}(t_{\mathcal{K}})\big\| \tag{54}$$

are recorded and subsequently used to compute evaluation metrics across all trajectories.

**Note:** Although each measurement provides only a scalar range, velocity information is implicitly recovered through temporal coupling in the CV(2) model. Over successive time steps, the EKF integrates

multiple nonlinear range measurements along with the process model, enabling velocity to be inferred from the evolution of position estimates. In environments where the beacon geometry ensures good observability, range-only updates are therefore sufficient to obtain accurate estimates of both position and velocity, provided that the beacon configuration avoids degeneracy and maintains consistent visibility throughout the motion.[11]

This CD–EKF, combined with the LOS-aware measurement model, forms the state-estimation algorithm used to evaluate every candidate beacon layout in the subsequent optimization.

## OBJECTIVE FUNCTION

The quality of a beacon configuration resulting from Eq. (13) is then evaluated by propagating the CD-EKF along the full set of trajectories. To avoid transient effects associated with filter initialization, the first $\Lambda$ fraction of samples is treated as a burn-in interval. Letting $s = 1, \ldots, N_{\mathrm{traj}}$ be the trajectory index and $\mathrm{b}_{frac} = \lfloor \Lambda M_{\mathrm{eval}} \rfloor$, we can define the tail error sequence:

$$\mathcal{E}^{(s)} = \left\{ e_{r,\mathcal{K}}^{(s)} \,\middle|\, b = \mathrm{b}_{frac}, \ldots, M_{\mathrm{eval}} \right\} \tag{55}$$

For each trajectory $s$, the robust position error metric is the $q$-th percentile of this tail distribution:

$$P_q^{(s)}(\mathbf{z}) = \mathrm{percentile}_q\big(\mathcal{E}^{(s)}\big) \tag{56}$$

with $q = 99$ in all results shown in this paper. The baseline cost $J_{\mathrm{base}}$ is chosen as the worst-case $P_{99}$ over all trajectories:

$$J_{\mathrm{base}}(\mathbf{z}) = \max_{s=1,\ldots,N_{\mathrm{traj}}} P_{99}^{(s)}(\mathbf{z}) \tag{57}$$

This definition explicitly emphasizes robustness: any beacon layout that performs poorly on even a single trajectory in the tube is penalized through a large value of $J_{\mathrm{base}}$. The LOS constraints enter through the EKF measurement model. Thus, poor beacon layouts that frequently self-occlude naturally produce larger values of $J_{\mathrm{base}}(\mathbf{z})$. The total objective function is then defined as:

$$J(\mathbf{z}) = J_{\mathrm{base}}(\mathbf{z}) + J_{\mathrm{reg}}(\mathbf{z}) \tag{58}$$

where $J_{\mathrm{reg}}(\mathbf{z})$ is regularization term defined in Eq. (11). The beacon-placement problem is posed as a nonlinear programming problem:

$$\min_{\mathbf{z} \in \mathbb{R}^{2KN_b}} J(\mathbf{z}) \tag{59}$$

where LOS effects are enforced implicitly through the occlusion-aware EKF evaluation used to compute $J_{\mathrm{base}}(\mathbf{z})$.

## NUMERICAL OPTIMIZATION STRATEGY

The beacon-placement problem in Eq. (59) is a smooth but highly nonconvex nonlinear program in the CSP–DG decision vector $\mathbf{z} \in \mathbb{R}^{2KN_b}$. The cost $J(\mathbf{z})$ couples the differentiable CSP–DG mapping and the LOS-aware EKF, while the minimum-spacing requirement between beacons appears as a nonlinear inequality constraint. To solve this problem, MATLAB's gradient-based interior-point solver `fmincon` is used together with a multi-start strategy and a sweep over the number of beacons.

For each fixed number of beacons $N_b$, the optimization problem:

$$\min_{\mathbf{z} \in \mathbb{R}^{2KN_b}} J(\mathbf{z}) \quad \text{subject to} \quad g_{il}(\mathbf{z}) \;\le\; 0, \qquad 1 \le i < l \le N_b \tag{60}$$

is solved using `fmincon` with the interior-point algorithm.

### Multi-start strategy and sweep over the number of beacons

The nonconvexity of Eq. (60) arises from both the nonlinear EKF performance metric and the mixture structure of the CSP–DG parameterization. To mitigate the risk of converging to poor local minima, a multi-start strategy is employed for each beacon count $N_b$.

Let $\mathcal{N} = \{N_{\min}, \ldots, N_{\max}\}$ denote the set of candidate beacon counts. For each $N_b \in \mathcal{N}$, the solver is run from $N_{\text{start}}$ distinct initializations:

$$\mathbf{z}_0^{(m)}, \qquad m = 1, \ldots, N_{\text{start}} \tag{61}$$

The best solution among these runs is retained:

$$J^*(N_b) = \min_{m=1,\ldots,N_{\text{start}}} J\left(\mathbf{z}^{(m)*}\right) \tag{62}$$

$$\mathbf{z}^*(N_b) = \arg\min_{m=1,\ldots,N_{\text{start}}} J\left(\mathbf{z}^{(m)*}\right) \tag{63}$$

where $\mathbf{z}^{(m)*}$ is the local optimum reached from initialization $\mathbf{z}_0^{(m)}$. Each multi-start initialization $\mathbf{z}_0^{(m)}$ is constructed beacon-by-beacon to encourage exploration of distinct regions of the rail network and to break the inherent symmetries of the plus-shaped perimeter.

### Evaluation Metrics and Selection Criteria

Selecting an appropriate performance metric is critical for LOS–aware beacon placement, as the geometry is often constrained by sharp occlusion boundaries and asymmetric visibility patterns. A RMS based metric tends to be overly optimistic in this setting, because it averages estimation error across the entire trajectory and thus masks short but severe degradations that occur when the observable subspace collapses. Such collapses arise naturally in LOS-limited configurations, where the spacecraft may momentarily lose access to a sufficient number of beacons or experience poor geometric diversity. As a result, two layouts with similar RMS performance can have dramatically different behavior in the tail of the error distribution, meaning RMS provides little insight into robustness under the worst combinations of pose, visibility, and beacon geometry. At the opposite extreme, using the raw maximum error as a metric is overly pessimistic and numerically brittle: a single linearization defect, momentary occlusion, or transient filter mismatch can dominate the objective, causing the optimizer to respond to isolated outliers that are not representative of overall estimation quality. This sensitivity makes raw max unsuitable for a smooth gradient-based optimization framework such as CSP–DG.

In contrast, the $P_{99}$ position error provides a principled balance between these two extremes by capturing the behavior of the error distribution's upper tail without being dominated by isolated anomalies. Because LOS occlusions tend to produce short-duration but meaningful spikes in estimation error, the $P_{99}$ metric directly incentivizes beacon layouts that maintain geometric observability even during challenging segments of the trajectory tube. Furthermore, taking the worst-case $P_{99}$ across all trajectories ensures that the selected configuration is robust to variability in spacecraft motion, initialization discrepancies, and local visibility constraints. For these reasons, the $P_{99}$ position error is the most appropriate and informative metric for evaluating and optimizing beacon placement within the CSP–DG framework.

The final design then selects the smallest $N_b$ whose robust error satisfies a prescribed tolerance $P_{99}^{\text{target}}$:

$$N_b^* = \min\left\{N_b \in \mathcal{N} \;\middle|\; \widehat{P}_{99}(N_b) \le P_{99}^{\text{target}}\right\} \tag{64}$$

with a fallback choice of the $N_b$ yielding the smallest $\widehat{P}_{99}(N_b)$ if no candidate meets the target.

## RESULTS

This section presents the numerical results of the LOS–aware beacon placement optimization performed on the space telescope geometry introduced previously. All evaluations use the full trajectory tube of 100 servicing trajectories.

A conservative COTS range sensor noise level of $\sigma_r = 0.05$ m is used throughout all simulations, consistent with the performance envelope of modern commercial solid-state time-of-flight sensors such as the Garmin LIDAR-Lite.[35] Process uncertainty is modeled with a white–acceleration spectral density of $q_a = 10^{-8}\ \mathrm{m}^2/\mathrm{s}^5$, representing a pessimistic upper bound suitable for robustness studies. The CSP–DG relaxation parameters are fixed to $T_{\mathrm{softmax}} = 0.1$, $\eta_{\mathrm{ent}} = 50$, $\eta_{\mathrm{diffuse}} = 50$, which encourage sharp but numerically stable softmax mixtures, ensuring that each beacon concentrates its probability mass on a single rail. A minimum spacing constraint of $d_{\min} = 5$ m is enforced to avoid clustered or mechanically infeasible layouts.

The objective is to determine the smallest number of beacons $N_b$ whose LOS–aware $P_{99}$ position error does not exceed the target threshold of 0.10 m. Figure 6 shows the resulting $P_{99}$ position and velocity errors as the Pareto front for $N_b = 1, \ldots, 10$. The sharp reduction in error from $N_b = 1$ to $N_b = 4$ reflects the improved geometric diversity provided by additional viewing baselines, while the diminishing improvement beyond $N_b = 6$ is consistent with observability saturation in range–only sensing. The smallest $N_b$ satisfying the target is $N^* = 7$ with $P_{99}$ position error of 0.0492 m and $P_{99}$ velocity error of 0.0025 m/s. Figure 7 shows the resulting beacon placement on the rail structure and the overall geometric configuration. All beacons are assigned cleanly to a single rail. These results show that the CSP–DG relaxation converges to a fully discrete solution, while maintaining smooth differentiability during optimization.

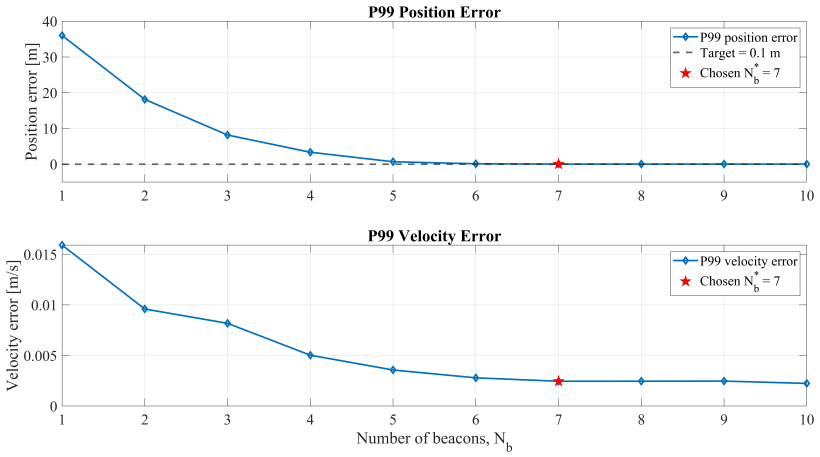


**Figure 6**: $P_{99}$ position and velocity errors versus number of beacons.

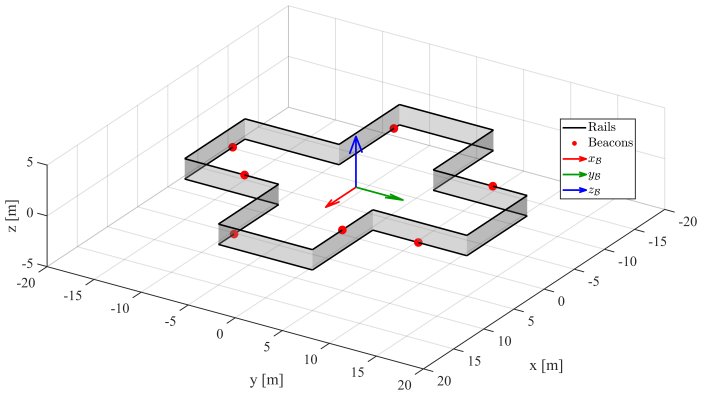


**Figure 7**: Chosen seven–beacon configuration on the perimeter rails.

The numerical results shown in Fig. 6 and demonstrate that the proposed LOS–aware CSP–DG formulation reliably identifies geometrically diverse and mechanically feasible beacon configurations on a complex, nonconvex spacecraft surface. Using conservative COTS sensor assumptions and a full trajectory tube, the

method converges to a discrete, unambiguous seven–beacon layout that meets the stringent $P_{99} \leq 0.10$ m position–accuracy requirement. The relaxation metrics confirm that the final solution is fully discrete with no ambiguity in rail assignment, and the resulting placement achieves sub–5 cm position accuracy and millimeter–per–second velocity accuracy across 100 servicing trajectories. These results demonstrate the robustness and practical viability of CSP–DG for real spacecraft navigation geometry design under strict LOS and hardware constraints.

The seven–beacon configuration shown in Fig. 7 exhibits several geometric features that align with intuitive LOS and observability requirements for range–only navigation. First, the beacons distribute themselves on both the top and bottom rails and across all four quadrants of the plus–shaped sunshield, ensuring multiple noncollinear baselines for any spacecraft pose encountered within the trajectory tube. This wide spatial separation directly reduces GDOP, particularly in regions where the spacecraft moves close to the structure or transitions across its lateral extents. Second, the layout avoids clustering even without any explicit regularization beyond the minimum–spacing constraint. The resulting positions lie near corners or long edges where LOS visibility is maximized, effectively leveraging structural protrusions to expand the viewing envelope. This behavior highlights the value of CSP–DG's continuous parameterization, which allows the optimizer to explore candidate positions along entire rail segments before converging to discrete solutions.

Overall, the final configuration reflects a careful balance between LOS visibility, geometric diversity, and mechanical feasibility, illustrating how the proposed CSP–DG formulation naturally yields navigation-favorable and physically realistic beacon geometries on complex spacecraft surfaces.

### Comparison with Random Beacon Placement

To quantify the benefit of the proposed CSP–DG beacon placement algorithm with explicit LOS constraints, a baseline comparison is performed against randomly placed beacons on the same admissible rail geometry. In this baseline, the number of beacons is fixed to $N_b = 7$, matching the optimal beacon count identified by the CSP–DG optimization, and beacon locations are sampled uniformly along the permissible rail segments while enforcing LOS feasibility. Figure 8 illustrates one such random seven–beacon configuration. Although all beacons satisfy the same geometric mounting as the optimized solution, their spatial distribution is not optimized for LOS visibility and estimation performance.

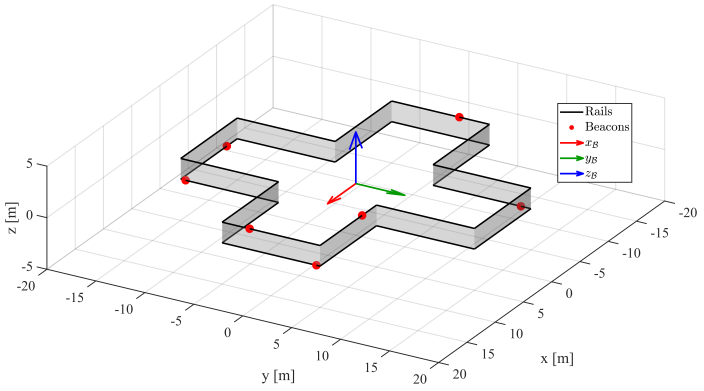


**Figure 8**: Random seven–beacon configuration on the admissible perimeter rails.

The resulting estimation accuracy degradation is substantial. For the random placement case, the EKF exhibits a worst–case $P_{99}$ position error of approximately 11 m and a $P_{99}$ velocity error of approximately 0.02 m/s. In contrast, the LOS-aware CSP–DG optimized configuration achieves a $P_{99}$ position error of 0.0492 m and a $P_{99}$ velocity error of 0.0025 m/s, as shown in Fig. 6. This corresponds to an improvement of over two orders of magnitude in robust position accuracy and nearly an order of magnitude in velocity accuracy for the same beacon budget. These results clearly demonstrate that enforcing LOS constraints alone is insufficient and that the geometric arrangement of beacons plays a significant role in estimation robustness.

The CSP–DG and ellipsoidal LOS constraint formulation developed in this work places beacons in locations that maximize information across all trajectories. Random placement, even when feasible, leads to poorly conditioned measurement geometry, reduced observability, and significantly degraded estimation performance. Overall, this comparison highlights that the proposed LOS-aware CSP–DG framework is not merely a refinement over heuristic placement strategies, but a necessary component for achieving mission-level estimation accuracy in complex, occluded spacecraft environments.

## CONCLUSIONS

This paper presented a LOS-aware optimization framework for beacon placement on structurally complex spacecraft, with application to relative navigation during proximity operations. A CSP–DG formulation was introduced to enable gradient-based optimization over a discrete rail network while preserving physical mounting constraints. LOS occlusions caused by the sunshield and primary mirror were modeled using a union of convex ellipsoids and evaluated using a numerically robust constrained-minimum test on ray–ellipsoid quadratics. Candidate beacon layouts were assessed through a CD–EKF using realistic sensor noise and a robust worst-case $P_{99}$ position error metric across a dense tube of approach trajectories. For the considered telescope geometry, the proposed method converged to a fully discrete seven-beacon configuration that achieved sub–10 cm worst-case position accuracy across all trajectories, outperforming random feasible placements by orders of magnitude. The proposed methodology applies across diverse geometric configurations and supports a wide range of ISAM and inspection missions involving large spacecraft with complex occluding geometries.

## ACKNOWLEDGMENTS

The authors acknowledge support from the Air Force Office of Scientific Research (AFOSR) under award number FA9550-24-1-0219.

## REFERENCES

[1] J. H. Saleh, E. S. Lamassoure, D. E. Hastings, and D. J. Newman, "Flexibility and the Value of On-Orbit Servicing: New Customer-Centric Perspective," *Journal of Spacecraft and Rockets*, Vol. 40, No. 2, 2003, pp. 279–291, 10.2514/2.3944.

[2] NASA, "On-orbit Servicing, Assembly, and Manufacturing 1 (OSAM-1)," `https://www.nasa.gov/mission/on-orbit-servicing-assembly-and-manufacturing-1/`, 2023. Accessed: 2024-02-21.

[3] J. A. Christian and E. G. Lightsey, "Review of Options for Autonomous Cislunar Navigation," *Journal of Spacecraft and Rockets*, Vol. 46, No. 5, 2009, pp. 1023–1036, 10.2514/1.42819.

[4] A. Hussain, F. Akhtar, Z. H. Khand, A. Rajput, and Z. Shaukat, "Complexity and Limitations of GNSS Signal Reception in Highly Obstructed Enviroments," *Engineering, Technology & Applied Science Research*, Vol. 11, Apr. 2021, p. 6864–6868, 10.48084/etasr.3908.

[5] R. Bommena and R. Woollands, "Indirect Trajectory Optimization with Path Constraints for Multi-Agent Proximity Operations," *The Journal of the Astronautical Sciences*, Vol. 71, No. 6, 2024, p. 54, 10.1007/s40295-024-00470-7.

[6] R. Bommena and R. Woollands, "Path-constrained optimal 6-DOF motion for multi-agent in-space servicing and assembly," *Acta Astronautica*, Vol. 238, 2026, pp. 91–102, https://doi.org/10.1016/j.actaastro.2025.08.052.

[7] R. Bommena, H. Panag, and R. Woollands, "Optimal 6-DOF Control for Servicing and Assembly at Sun-Earth L2," *Journal of Guidance, Control, and Dynamics*, 2025 [under review].

[8] M. Rognant, C. Cumer, J.-M. Biannic, M. A. Roa, A. Verhaeghe, and V. Bissonnette, "Autonomous assembly of large structures in space: a technology review," *EUCASS 2019*, Madrid, Spain, July 2019.

[9] D. C. Woffinden and D. K. Geller, "Observability Criteria for Angles-Only Navigation," *IEEE Transactions on Aerospace and Electronic Systems*, Vol. 45, No. 3, 2009, pp. 1194–1208, 10.1109/TAES.2009.5259193.

[10] J. L. Crassidis and J. L. Junkins, *Optimal Estimation of Dynamic Systems*. New York: Chapman and Hall/CRC, 2nd ed., 2011, 10.1201/b11154.

[11] J. A. Christian, "Relative Navigation Using Only Intersatellite Range Measurements," *Journal of Spacecraft and Rockets*, Vol. 54, No. 1, 2017, pp. 13–28, 10.2514/1.A33608.

[12] G. Gaias, S. D'Amico, and J.-S. Ardaens, "Angles-Only Navigation to a Noncooperative Satellite Using Relative Orbital Elements," *Journal of Guidance, Control, and Dynamics*, Vol. 37, No. 2, 2014, pp. 439–451, 10.2514/1.61494.

[13] S. Theil and L. Bora, "Beacons for supporting lunar landing navigation," *CEAS Space Journal*, Vol. 9, No. 1, 2017, pp. 77–95, 10.1007/s12567-016-0132-6.

[14] C. Toldbo, A. Kiss, N. Törjék, C. A. Vázquez, D. L. Bényei, and M. Therkelsen, "Deployment Method and Optimal Placement of Surface Beacon Navigation System for Co-located Lunar Landings," *Acta Astronautica*, Vol. 193, 2022, pp. 432–443, https://doi.org/10.1016/j.actaastro.2022.01.003.

[15] Z. Zhang, L. Deng, J. Feng, L. Chang, D. Li, and Y. Qin, "A Survey of Precision Formation Relative State Measurement Technology for Distributed Spacecraft," *Aerospace*, Vol. 9, No. 7, 2022, 10.3390/aerospace9070362.

[16] J. Jeong, S. Kim, and J. Suk, "Parametric study of sensor placement for vision-based relative navigation system of multiple spacecraft," *Acta Astronautica*, Vol. 141, 2017, pp. 36–49, https://doi.org/10.1016/j.actaastro.2017.09.020.

[17] J. McGuire, Y. W. Law, J. Chahl, and K. Doğançay, "Optimal Beacon Placement for Self-Localization Using Three Beacon Bearings," *Symmetry*, Vol. 13, No. 1, 2021, 10.3390/sym13010056.

[18] E. Sequeira, H. Saad, S. Kelly, and M. Giamou, "Towards Optimal Beacon Placement for Range-Aided Localization," *ArXiv*, Vol. abs/2405.11550, 2024.

[19] S. Casini, A. Cervone, B. Monna, and E. Gill, "On line-of-sight navigation for deep-space applications: A performance analysis," *Advances in Space Research*, Vol. 72, No. 7, 2023, pp. 2994–3008. Space Environment Management and Space Sustainability, https://doi.org/10.1016/j.asr.2022.12.017.

[20] D. B. Jourdan and N. Roy, "Optimal sensor placement for agent localization," *ACM Trans. Sen. Netw.*, Vol. 4, June 2008, 10.1145/1362542.1362544.

[21] I. G. Velentzas, M. Dor, and P. Tsiotras, *A Robust Monocular Line-based Relative Navigation Approach for Spacecraft Rendezvous and Proximity Operations*, 10.2514/6.2024-0434.

[22] T. Chen and S. Xu, "Double line-of-sight measuring relative navigation for spacecraft autonomous rendezvous," *Acta Astronautica*, Vol. 67, No. 1, 2010, pp. 122–134, https://doi.org/10.1016/j.actaastro.2009.12.010.

[23] J. O. Woods and J. A. Christian, "Lidar-based relative navigation with respect to non-cooperative objects," *Acta Astronautica*, Vol. 126, 2016, pp. 298–311. Space Flight Safety, https://doi.org/10.1016/j.actaastro.2016.05.007.

[24] E. Tongco and D. Meldrum, "Optimal sensor placement of large flexible space structures," *Journal of Guidance, Control, and Dynamics*, Vol. 19, No. 4, 1996, pp. 961–963, 10.2514/3.21725.

[25] D. Moreno-Salinas, A. M. Pascoal, and J. Aranda, "Optimal Sensor Placement for Multiple Target Positioning with Range-Only Measurements in Two-Dimensional Scenarios," *Sensors*, Vol. 13, No. 8, 2013, pp. 10674–10710, 10.3390/s130810674.

[26] S. Gao, W. Wei, Y. Zhong, and Z. Feng, "Rapid alignment method based on local observability analysis for strapdown inertial navigation system," *Acta Astronautica*, Vol. 94, No. 2, 2014, pp. 790–798, https://doi.org/10.1016/j.actaastro.2013.10.003.

[27] Y. Teng and J. Wang, "A closed-form formula to calculate geometric dilution of precision (GDOP) for multi-GNSS constellations," *GPS Solutions*, Vol. 20, No. 3, 2016, pp. 331–339, 10.1007/s10291-015-0440-x.

[28] A. Gelb, *Applied Optimal Estimation*. Cambridge, MA: MIT press, 1974.

[29] J. L. Crassidis, F. L. Markley, and Y. Cheng, "Survey of Nonlinear Attitude Estimation Methods," *Journal of Guidance, Control, and Dynamics*, Vol. 30, No. 1, 2007, pp. 12–28, 10.2514/1.22452.

[30] M. Karpenko, J. T. King, C. J. Dennehy, and I. Michael Ross, "Agility Analysis of the James Webb Space Telescope," *Journal of Guidance, Control, and Dynamics*, Vol. 42, No. 4, 2019, pp. 810–821, 10.2514/1.G003816.

[31] S. Gold, A. Rangarajan, *et al.*, "Softmax to softassign: Neural network algorithms for combinatorial optimization," *Journal of Artificial Neural Networks*, Vol. 2, No. 4, 1996, pp. 381–399.

[32] C. E. Shannon, "A mathematical theory of communication," *The Bell System Technical Journal*, Vol. 27, No. 3, 1948, pp. 379–423, 10.1002/j.1538-7305.1948.tb01338.x.

[33] J. R. Quinlan, "Induction of decision trees," *Machine Learning*, Vol. 1, No. 1, 1986, pp. 81–106, 10.1007/BF00116251.

[34] M. Hubert, H. Panag, and R. Woollands, "Ellipsoidal Thruster Pointing Constrained Optimal Trajectories for Satellite Servicing at SEL2," *Proceedings of the AAS/AIAA Astrodynamics Specialist Conference*, Boston, MA, 2025.

[35] J. Delaune, R. Brockers, D. S. Bayard, H. Dor, R. Hewitt, J. Sawoniewicz, G. Kubiak, T. Tzanetos, L. Matthies, and J. Balaram, "Extended Navigation Capabilities for a Future Mars Science Helicopter Concept," *2020 IEEE Aerospace Conference*, 2020, pp. 1–10, 10.1109/AERO47225.2020.9172289.